Experimental Mechanics (2019) 59:1285–1297
https://doi.org/10.1007/s11340-018-00449-0

Numerical and Experimental Study of the Spatial Stress Distribution on the Cornea Surface During a Non-Contact Tonometry Examination

S. Muench[1,2,3] · M. Roellig[2,3] · E. Spoerl[4] · D. Balzani[5]

Received: 23 February 2018 / Accepted: 29 October 2018 / Published online: 12 December 2018

Abstract

The determination of biomechanical properties of the cornea by a non-contact tonometry (NCT) examination requires a precise knowledge of the air puff generated in the device, which is applied to the cornea surface. In this study, a method is proposed to identify the resulting stress profile on the surface, which may be used to numerically solve an inverse problem to obtain the material properties. This method is based on an experimental characterization of the air puff created by the Corvis ST in combination with computational fluid dynamic (CFD) simulations, which are adjusted to the experimental data. The identified nozzle inlet pressure of approximately 25 kPa (188.5 mmHg) is then used for a numerical influence study of the interaction between the air puff and the cornea deformation. Therefore, eleven cornea deformation states based on measurements are implemented in the CFD model. A more realistic model is also analyzed by the geometrical reproduction of the human face, which is used for a further influence study. The outcomes showed a dependence between the cornea deformation and the pressure as well as the shear stress distribution. However, quantitatively, the shear stress component can be considered of minor importance being approximately one hundred times smaller than the pressure. The examination with consideration of the human face demonstrates that the pressure and shear stress distributions are not rotationally symmetric in measurements on real humans, which indicates the requirement to include more complex stress distributions on the eye. We present the detailed stress distribution on the cornea during a non-contact tonometry examination, which is made accessible for further investigations in the future by analytical nonlinear functions.

Keywords Corneal biomechanics · Non-contact tonometry · Computational fluid dynamics · Pressure distribution · Shear force distribution · Air puff characterization

Introduction

Non-contact tonometry (NCT) has proven to be valuable for the determination of intraocular pressure (IOP) to diagnose several diseases and has the advantage of a non-destructive method. In this context an air puff is produced which induces a load on the cornea, the transparent front part of the exterior eye shell. The resulting deformation of the cornea is continuously measured by image analysis techniques and for the configuration in which the cornea is maximally flattened (applanated state) the IOP can be estimated from the applied pressure. Thereby, the stiffness of the cornea is assumed to be negligible. Furthermore, a vast amount of load-displacement data, which is available by this standard procedure, is not exploited. However, using this data and avoiding strong simplifications on the material level would provide the basis for an extension of this method

Electronic supplementary material The online version of this article (https://doi.org/10.1007/s11340-018-00449-0) contains supplementary material, which is available to authorized users.

✉ S. Muench
stefan.muench@ikts.fraunhofer.de

[1] Institute of Mechanics and Shell Structures (IMF), Dresden 01062, Germany

[2] Fraunhofer Institute for Ceramic Technologies and Systems (IKTS), Dresden 01109, Germany

[3] Dresden Center for Computational Materials Science (DCMS), Technische Universität Dresden, Dresden 01062, Germany

[4] Department of Ophthalmology, Medical Faculty Carl Gustav Carus, Technische Universität Dresden, 01307 Dresden, Germany

[5] Chair of Computational Mechanics, Ruhr-Universität Bochum, 44801 Bochum, Germany

to measure further biomechanical properties of the cornea linked with material properties such as collagen stiffness and distribution. Such parameters, obtained in vivo, would be a key towards an earlier and more precise diagnosis of many more eye diseases.

Many researchers and manufacturers have been working on such examination methods based on various techniques. What they all have in common is that they specifically stimulate the cornea to record a biomechanical response. Nevertheless, they differ in the type of stimulation and recording. Examples are Brillouin scattering [1], ultrasound (US) elasticity microscopy [2], air puff based NCT [3], electronic speckle pattern interferometry (ESPI) [4], optical coherence tomography (OCT) elastography [5], magnetic resonance elastography [6], supersonic shear imaging based methods [7] as well as methods using laser-induced surface acoustic waves [8].

However, the NCT is currently the only clinical device used for the determination of biomechanical properties on the structural level of the eye. Today, two devices are available, the ocular response analyzer (ORA) by Reichert Inc. (Buffalo, USA) and the Corvis ST by Oculus Optikgeräte GmbH (Wetzlar, Germany), which are used as experimental basis for researchers working on the inverse identification of biomechanical material properties [9, 10] using finite elements (FE) to compute the mechanical fields inside the cornea. Nevertheless, a FE-simulation requires boundary conditions such as the correct loading on the cornea surface applied through the air puff. The short examination duration of approximately 30 ms used in both devices makes it difficult to quantitatively characterize the air puff, and thus appropriate boundary conditions. These short duration is however necessary to ensure an examination which is as pleasant as possible for the patient. Typically, strong assumptions regarding the load profile are made, although a high accuracy of the identified biomechanical properties is desired. The correct modeling of the pressure and shear stress distribution is thus an essential requirement for a conclusive simulation. Experimental investigations [11], computational fluid dynamic (CFD) simulations [12–14] or coupled analysis [15] have not yet resulted in realistic stress distributions because the influence of deformed eye configurations and the surrounding structure given by the face geometry on the stress distribution on the eye surface have not been taken into account. Therefore, here we present a detailed CFD analysis where we analyze these effects, such that more realistic stress distributions on the cornea are identified. The simulations are calibrated to an experimental measurement and mathematical functions describing the resulting distributions are provided.

Materials and Methods

Dependencies of the pressure and shear distributions on cornea deformations and surrounding geometries were examined with CFD simulations. Here we focus on air puffs generated by the Corvis ST. Based on the assumption, that the device generates a reproducible air puff in every examination and that this air puff is independent on the particular Corvis ST device, exactly one time-dependent pressure profile has to exist describing the nozzle inlet boundary condition. This boundary condition was calibrated by inverse CFD modeling in combination with a pendulum experiment, cf. [16]. The main parameter investigated in the calibration process, was the experimentally obtained force applied to the pendulum in flow direction. The solution of inverse problems in determining the material properties of the cornea based on complete simulations of the air flow and eye deformation using FSI simulations would not allow patient-specific analysis in clinical practice due to the expense of computational time. For the investigation of the deformation dependence of the stress distributions, a procedure is proposed which avoids fluid structure interaction (FSI) simulations. The stress distribution on the corneal surface depends only on the resulting flow field, which, in turn, depends directly on the geometry of the streamed body. This means that exactly one stress distribution can be assigned to each corneal deformation state. Note that it does not matter whether the deformed geometry is based on soft material properties and a high intraocular pressure or vice versa.

Experimental Approach

As a calibration for the CFD simulations the boundary condition (pressure at the nozzle inlet) has to be identified. For this purpose an experiment was performed, where the air puff was applied to a rigid eye model, which was hung up through a yarn and positioned in front of the nozzle exit. Note that in the experiment a rigid body was used to eliminate any effects due to changes in the shape of the test body. The air puff induces the eye model to accelerate backwards and based on a measurement of the eye movement the required force was calculated. This force was then considered as boundary condition to an inverse problem where the required time-dependent pressure at the nozzle inlet was identified using CFD simulations.

Figure 1 shows the setup used for the pendulum investigation. The experiments were performed using a commercial Corvis ST containing the software version 1.3b1453. A sufficiently rigid glass eye (augenladen.de, Lauscha, Germany) was used as eye model to ensure a

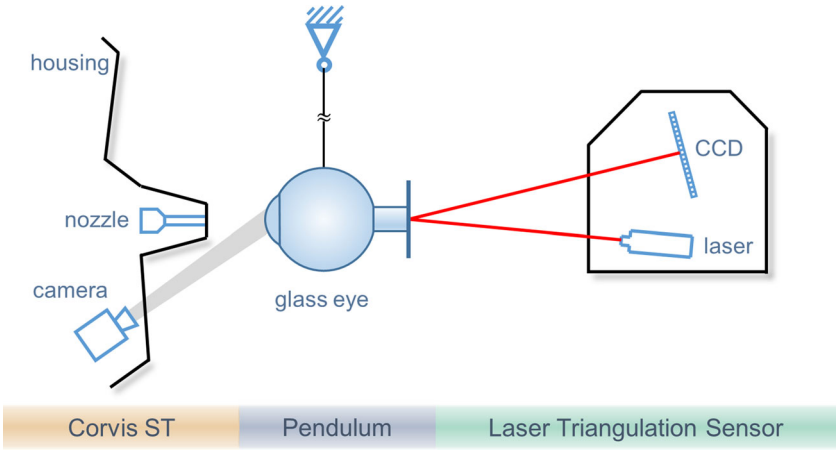

Fig. 1 Setup of the Pendulum Experiment consisting of the glass eye positioned in front of the Corvis ST and the laser triangulation sensor on the back of the glass eye to record a high-resolution movement time curve

good result portability to real eyes and to avoid interfering influences by deformations.

The glass eye was attached to a 31 cm long yarn and positioned in a distance of $L1 = 11$ mm from the nozzle exit (the typical examination distance). Similar to the human eye, the used glass eye has an averaged scleral diameter of $D1 = 24$ mm, a corneal diameter of $D2 = 12$ mm and an anterior curvature of $R1 = 8.2$ mm. A laser triangulation sensor (optoNCDT 2300-20, Micro-Epsilon, Ortenburg, Germany) was positioned in the back of the glass eye to measure its movement induced by the air puff. This sensor operates with a resolution of 0.3 µm and a frequency of 20 kHz, high enough to monitor the fast reaction on the air puff [17]. The movement-time data recorded by the laser triangulation sensor was imported into OriginPro 2016G and masked to the field of interest. The standard deviation of three repeat measurements was approximately 15 µm. Next the data was numerically derived from movement-time to acceleration-time-curve and processed by a Savitzky-Golay filter with second-order polynomial fit about a range of 4.95 ms to remove coarse noise. In a second step, a parabolic low-pass filter was used to eliminate high frequent oscillations. Finally, the glass eye weight of 6.5 g was multiplied and the force-time-curve was obtained.

Computational Fluid Dynamic Model

The air puff development and its interaction with the solid geometries was studied in CFD simulations, performed with the software ANSYS 16.1 CFX. In accordance with the experimental setup, a three-dimensional model was built, shown in Fig. 2 based on the dimensions presented in Table 1. It was simplified to a double symmetric model for reasons of accelerated computing times.

Developing a velocity profile, the air is flowing through the cylindrical nozzle with a length of $L2 = 24$ mm and an inner radius of $R2 = 1.2$ mm. Leaving the nozzle exit, the airflow impinged the rotationally symmetrical glass eye geometry. To model the glass eye, two rigid intersecting spheres were considered which represent the

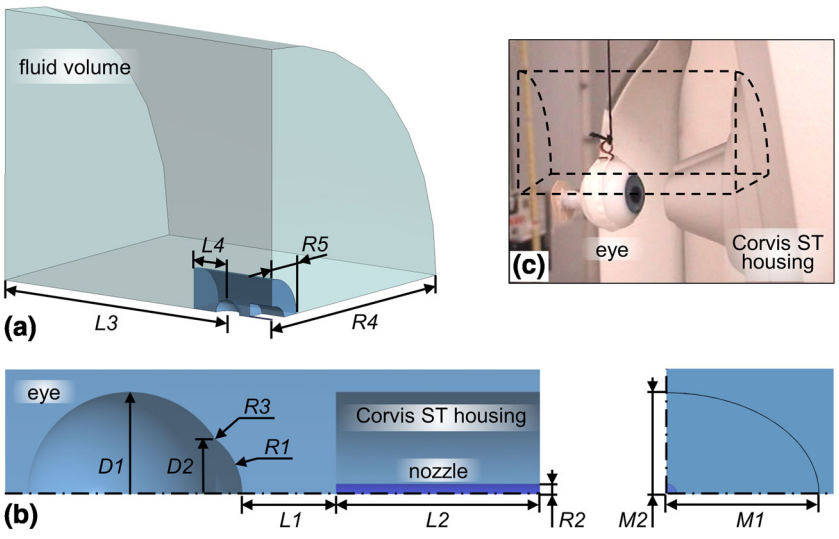

Fig. 2 **a** Dimensioned CFD model of the glass eye in isometric view and **b** details of the inner volume in front and side view compared to **c** the physical model. The corresponding parameter dimensions are shown in Table 1

Table 1 Parameter dimensions used in the double-symmetrical model

Parameter	$D1$	$D2$	$L1$	$L2$	$L3$	$L4$	$M1$	$M2$	$R1$	$R2$	$R3$	$R4$	$R5$
Value [mm]	24	12	11	24	240	36	18	12	8.2	1.2	0.5	240	36

spherical cornea body and an added spherical sclera body. The sharp edge between the spheres was rounded by a chamfer with a radius of $R3 = 0.5\,\text{mm}$. An ellipsoidal cylinder with a horizontal semi-major of $M1 = 18\,\text{mm}$ and a vertical semi-minor of $M2 = 12\,\text{mm}$ partly reproduces the nozzle enclosure of the device. The distance between the sclera center and the computational domain boundaries ($L3$, $R4$) were set to 10 times the scleral diameter ($10 \cdot D1 = 240\,\text{mm}$), based on a perturbation study. To ensure a controlled grid generation, the fluid domain was split into two volumes. An inner volume $1.5 \cdot D1$ around the center of the eye and a remaining outer volume.

In order to model a low surface roughness, the surfaces of the nozzle and the glass eye were configured as smooth walls, while the surfaces representing the Corvis ST enclosure were set to free slip walls. An internal pressure sensor records the pressure generated in the Corvis ST. This measured pressure-time-curve is set as the nozzle inlet multiplied with a self-defined parameter, called pressure reduction factor (PRF). At the symmetry planes, symmetric boundary conditions were applied and the remaining faces were considered as open boundaries. A CFD analysis is based on the partial differential conservation equations of mass, momentum and energy, well known as Navier-Stokes equations. Furthermore, the high flow velocity expected in the simulation requires the consideration of compressibility effects and thus here an ideal gas is considered. The calculations of turbulent flows were done by approximations in form of turbulence models using the shear stress transport (SST) model. It has a modified eddy-viscosity definition compared to the baseline model, which itself blends the $k-\epsilon$ with the $k-\omega$ model in near wall regions [18]. To solve the set of equations the CFD-code CFX uses the finite volume method. It integrates the equations over control volumes and uses the Gauss divergence theorem to convert appropriate volume integrals to surface integrals, which consists of summed fluxes of the considered values across the control volume surface [19]. While the pressure gradient and the diffusive terms were evaluated with FE-shape functions, the advection terms were discretized by different discretization schemes. The authors chose the high resolution scheme for discretization, which blends between 0 (1st order upwind) and 1 (central difference scheme) with the attempt to use a blend close to 1 if possible. For the consideration of time the 2nd order backward euler scheme was used for the approximation of the transient term. The mass flow terms contain a non-constant density because of the compressibility, and thus, a Newton-Raphson linearization was used by the CFD-code for discretization instead of the pressure-velocity-coupling, which is typically used for incompressible flows. These discretized equations were then solved iteratively until the predefined root mean square (RMS) convergence criterion with a tolerance of $1 \cdot 10^{-4}$ was satisfied. A numerical study showed that there was no significant effect on the results when using tolerances between $1 \cdot 10^{-4}$ and $1 \cdot 10^{-5}$, but a large impact on the computational time was obtained. An adaptive time step control for the transient problem was used making sure that convergence was obtained for each time step. This specified numerical solution setup is summarized in the appendix, see S1 Table. The finite volumes constructed in ANSYS CFX were based on a FE-mesh. A detailed description about this method can be found in the ANSYS documentation [19]. Because this finite volume method is element-based, in the following the finite volumes are referred to as elements. The computational domain was meshed with tetrahedral elements using three different mesh settings. An extremely dense setting was used for regions were high gradients were expected, like the nozzle volume, the flow path from nozzle exit to stagnation point and the glass eye surfaces. In these regions, a defined element size E_{dense} was considered. A fine setting was applied to the inner volume with the parameters E_{fine} and a growth rate $G_{\text{fine}} = 1.1$ (factor describing how strong the element size may change over position). In the outer volume the coarsest setting was considered, where the growth rate was set to $G_{\text{std}} = 1.2$. Zones near the walls and around the eye were discretized using prism layers and zones inside the nozzle by using hexahedral elements for accurate boundary layer calculations. This boundary layer mesh is defined by the thickness of the first element slice Δy, the number of slices in the layer n_{BL} and the growth rate $G_{\text{BL}} = 1.2$ in normal direction of the layer surface. For the nozzle, the thickness of the first slice was set to $\Delta y \approx 25\,\mu\text{m}$ and the number of slices $n_{\text{BL}} = 11$ was obtained by comparison of the fully developed velocity profile at nozzle outlet with the power law for boundary layers in tubes [20]. After an investigation of different parameters within a range of $1.2\,\mu\text{m} \leq \Delta y \leq 121.1\,\mu\text{m}$ and $2 \leq n_{\text{BL}} \leq 27$, a suitable discretization of the boundary layer around the eye was found as $\Delta y \approx 6\,\mu\text{m}$ and $n_{\text{BL}} = 15$. As recommended by the fluid engineering division of the American Association of Mechanical Engineers (ASME) [21], the grid convergence index (GCI) was used to quantify the quality of the finest grid. S2 Table given in the appendix summarizes the parameters of the three investigated grids. The GCI was computed for two quantities of interest, the stagnation point

pressure p_0 as a local control value and the resultant force as spatial integral of the forces on the eye in flow direction $F_{x,Eye}$ as global control value. The pressure at stagnation point and the resultant force show a good grid quality with a $GCI_{p0}^{fine} \approx 1.89\,\%$ and $GCI_{ForceEye}^{fine} \approx 0.84\,\%$. Thereby, the results of grid 3 were representing an accurate local and global mesh quality.

Experimental Calibration

For the calibration of the computational model, the time-dependent resultant force applied on the eye in flow direction was calculated for different PRF's. Figure 3 shows the resulting force-time curves. The comparison with the experimental curve reveals that the pressure at the nozzle inlet seems to be nearly identical with the pressure measured by the Corvis ST internal sensor. It means that the loss of kinetic energy in the tube between the pressure chamber and the sensor was almost the same as between the chamber and the nozzle inlet. Figure 3 shows furthermore a qualitatively identical time response. Consequently, the pressure imposed at the nozzle inlet over time is taken from the pressure-time curve measured with the Corvis ST internal sensor, which reaches its maximal pressure of approximately 25 kPa at about 17.5 ms.

Incorporation of Deformation States Based on Measurements

To investigate the dependence of the stress distribution on the deformation, the sphere representing the cornea in the eye model considered above was replaced in the CFD model by a realistic shape of a human cornea. For this purpose, a spline defined by 27 construction points was rotated to form the new cornea shape. The coordinates of the construction points were obtained from a Corvis ST measurement of a healthy person. Within one measurement, the deformed states of the cornea are identified for 140 time frames and for the analysis performed here, 11 equidistant deformation states were selected and corrected by the rigid body motion of the whole eye. A symmetric in-plane deformation contour was forced by averaging the data points at the same radius, which is measured from the point of maximal indentation. Figure 4 illustrates the considered states.

For the simulations of the glass eye, the consideration of the tear film was not necessary. In the simulations of the human eye, also the tear film was not taken into account since its influence on the stress distribution is assumed negligible due to the small thickness of 4.79 μm [22].

Incorporation of Human Face

The human face surrounding the eye is also taken into account to investigate its influence on the stress distribution at the cornea surface resulting from the air puff. For this purpose, a model of the human face by XAMR [23] was scaled to natural dimensions in SolidWorks 2014, revised and transferred as surface model into the CFD simulation, where it was vertically cut in half and overlaid on the virtual eye. The axis of the fluid cylinder was moved to the cutting plane of the face and the cylinder itself was transformed to an elliptical cylinder totally encasing the face. Figure 5 shows the adapted model. Note, that the eyelashes were neglected.

Results

Dependency of the Deformation on the Cornea Stress Distribution

The schematic illustration in Fig. 6 shows the flow direction of the air puff. All velocity vectors were split into one

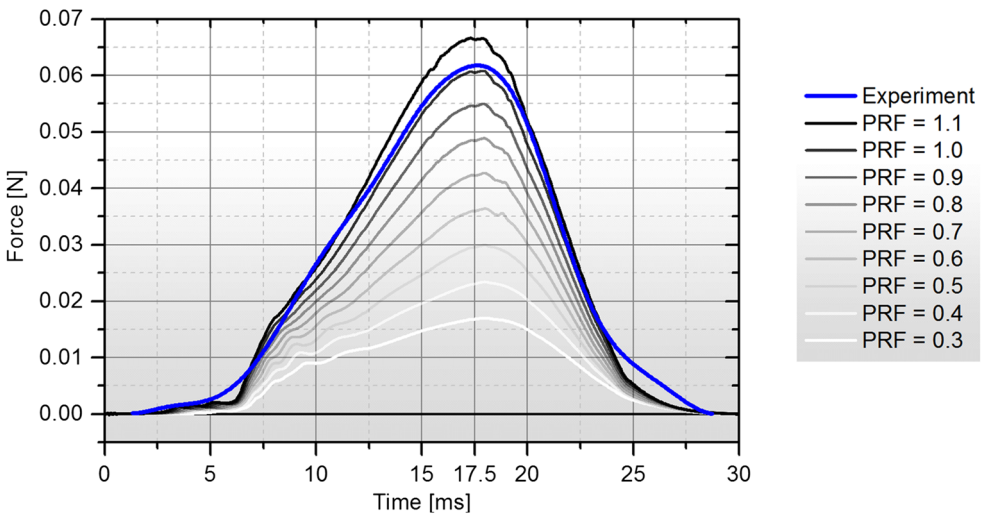

Fig. 3 Computed force-time curves from CFD simulations compared to the experimental curve

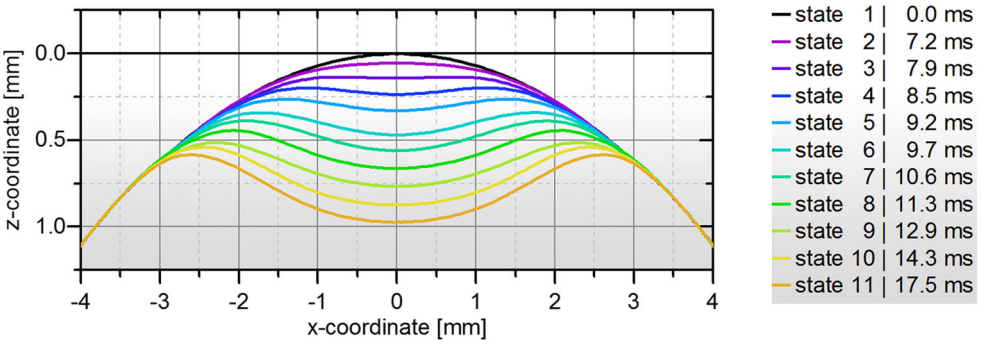

Fig. 4 Measured deformation states of a human cornea implemented in the CFD model

component perpendicular to the cornea contour and one tangential. The perpendicular component results in the pressure applied on the surface, whereby a component directed to the surface leads to a positive pressure and a component directed away from the surface to negative pressure. Negative pressure occurs if the fluid follows a concave contour like the peak in the deformed state. This explains the influence of the cornea contour and its deformation states on the cornea loading.

Figure 7 shows the dependency of the pressure distribution for the eleven simulated deformation states. As expected, the pressure is maximal in the cornea center and decreases rapidly with an increasing radial position. The minimum of the pressure marks the peak in the deformed state and the local maximum at a radius of approximately 6 mm marks the transition from cornea to sclera. After this transition, the flow follows the eye shape and the pressure component is negligible.

The tangential component of the velocity vectors result in shear stresses, also presented in Fig. 7. The stresses are subordinated by factor one hundred compared to the pressure, which was already found by Roy et al. [13]. The shear stresses are zero at the stagnation point and then increase with increasing radial position until they reach their maximum. Then they decrease based on the decreasing flow velocity along the eye.

The difference between the distribution curves for different deformation states was quantified by calculating the relative deviation f between the curves according to Eq. 1

$$f = \frac{\int_{0\,\mathrm{mm}}^{12\,\mathrm{mm}} |v_\mathrm{n}(r) - v_1(r)| dr}{\int_{0\,\mathrm{mm}}^{12\,\mathrm{mm}} |v_1(r)| dr}. \tag{1}$$

with the pressure or shear stress v at the radius r of the corresponding deformation state n compared to the

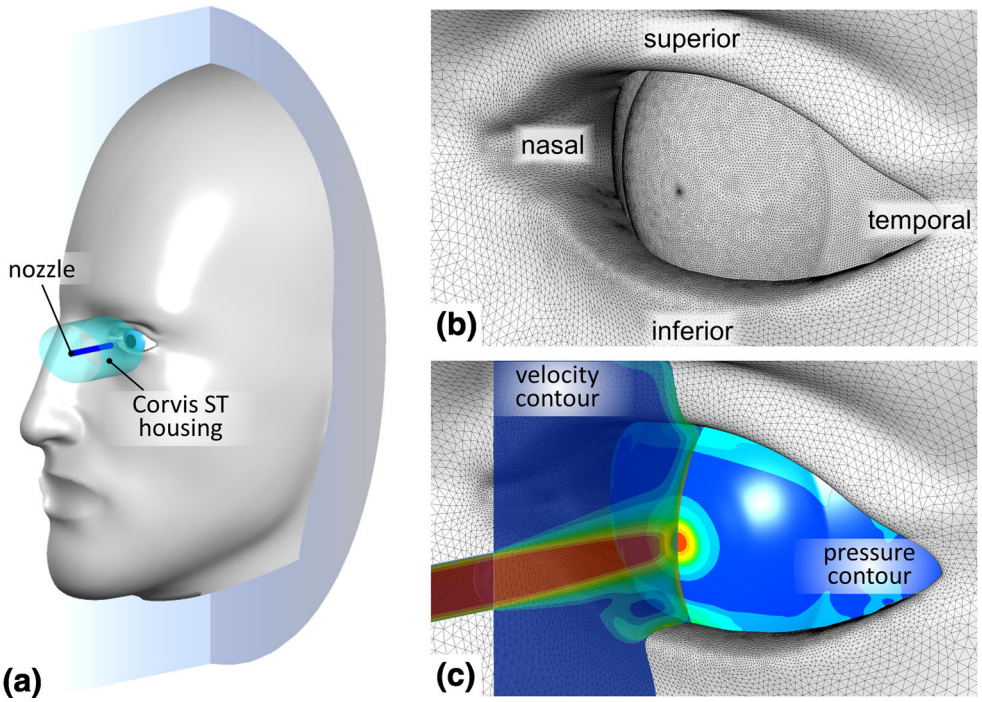

Fig. 5 Model with human face in **a** isometric model view, **b** detail view of the surface mesh and **c** detail view of the velocity and pressure distribution

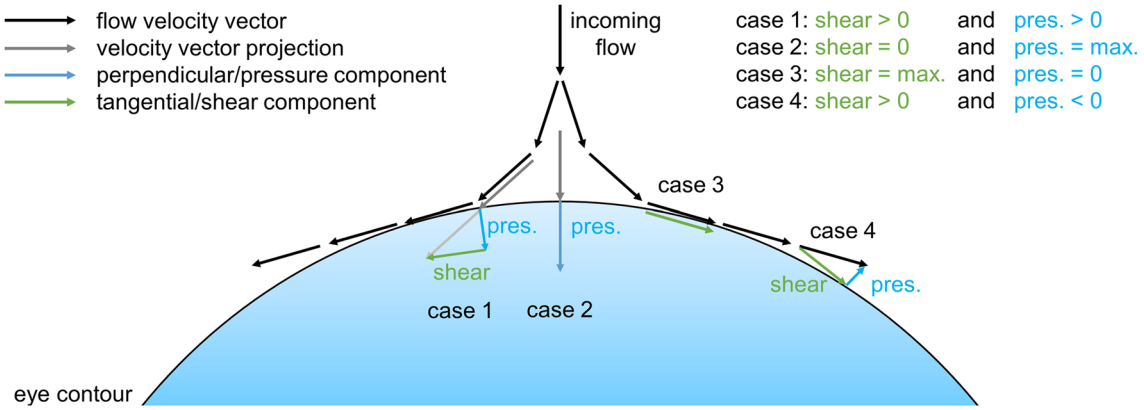

Fig. 6 Schematic representation of the velocity vectors perpendicular (pressure component) and parallel (shear component) to the cornea surface

undeformed state $n = 1$. The relative deviations for all eleven deformation states are presented in Table 2. Since most biomechanical markers of the Corvis ST system are calculated in the state of applanation (state 3) and in the state of maximum deformation (state 11), these states are most interesting.

The relative deviations between the undeformed state (state 1) and the applanated state (state 3) are small for both the pressure and the shear stress curves, so that the influence on the Corvis ST parameters on the applanated state is considered negligible. However, the relative deviations of the maximum deformed state (state 11) of up to 34 % show that the effect of the corneal deformation on the pressure and shear stress for deformation states beyond the applanation must be taken into account.

Influence of the Human Face on Corneal Loading

Based on the recent finding, that the deformation state significantly influences the loading, the question arises how the human face effects the loading. The pressure distributions in the nasal-temporal and in the inferior-superior

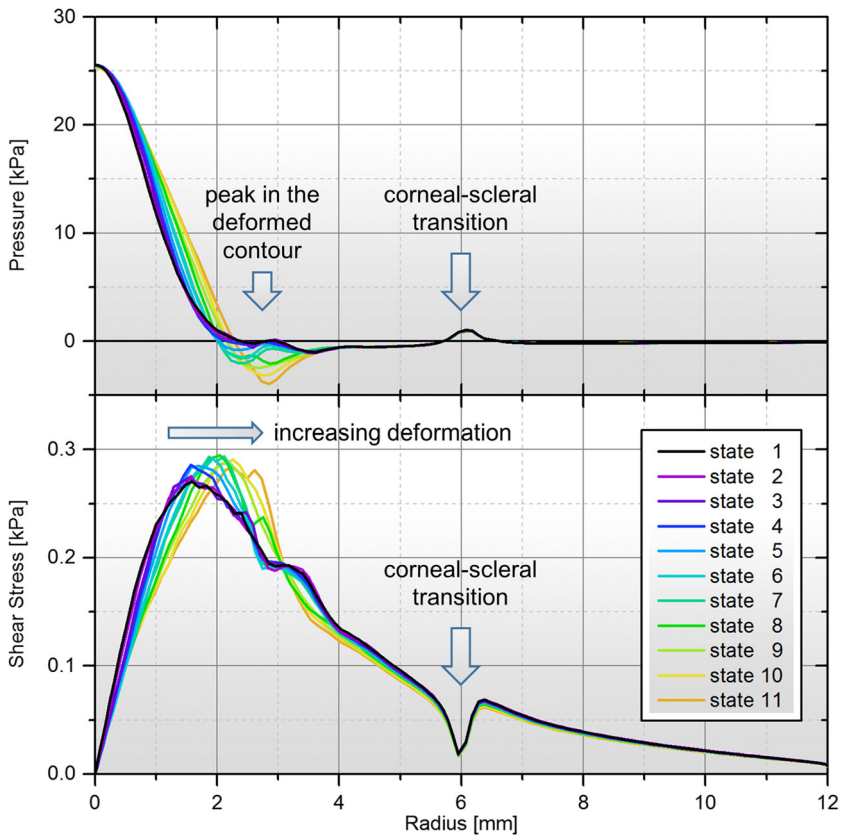

Fig. 7 Diagrams of pressure distribution and shear stress distribution on the corneal surface for all eleven deformation states

Table 2 Integrally based deviations of the deformation-dependent distribution curves

	Pressure		Shear	
State [−]	I_p [kPa mm]	f[%]	I_s [kPa mm]	f[%]
1	28.47	0.00	1.16	0.00
2	28.61	2.41	1.15	1.48
3	29.58	4.51	1.14	2.60
4	29.77	7.77	1.14	3.50
5	30.94	11.66	1.13	4.84
6	32.57	16.58	1.11	6.65
7	33.16	18.48	1.12	7.01
8	34.50	23.47	1.11	9.82
9	35.61	26.03	1.10	10.35
10	36.90	30.88	1.09	12.76
11	37.78	33.84	1.08	14.16

cut were extracted from the model and shown in the diagrams Fig. 8. Compared to the levitating eye, the distribution in the central cornea region is nearly identical. In contrast, the pressure distribution in the inferior-superior cut strongly increases in the edge regions up to approximately 40 % of the maximum value. This increase is based on the flow redirection evoked by the eyelid. Thus, the almond-shaped eyelids are leading to a not rotationally symmetrical pressure distribution. The different distances from the cornea center to the eyelids in the inferior-superior direction are leading furthermore to an asymmetric distribution along the cut itself, clearly recognizable in Fig. 8. The shear stress distributions in the nasal-temporal and inferior-superior cuts show a similar asymmetric behavior and are presented in Fig. 9.

The calculation of the relative deviations is done by Eq. 1. Table 3 presents the deviations between the results of the undeformed levitating eye and the results of the model with the surrounding face geometry along the cuts. As expected, all deviations increase by increasing cornea deformations and reach the largest values at the maximally deformed state 11. The deviation of the pressure curves along the nasal-temporal cut are however, approximately two times higher than in the inferior-superior.

In summary, the results show significant differences between the pressure and shear stress distributions considering the human face compared to the levitating eye. These differences grow by increasing cornea deformation.

Presentation of the Results as Simple Curve and Surface Functions

In FE simulations of NCT, the pressure and shear stresses determined in the CFD must be transferred to the element nodes. For this reason, suitable coordinate dependent functions were constructed. In the following, the function coefficients are determined, for which the functions best represent the results of the CFD simulations. A separate set of functional coefficients is determined for each state of the corneal deformation in order to take into account the dependency of deformations. Note, that the coefficients were determined for the maximal pressure of 25 kPa. To simulate the NCT, the results must be scaled according to the time-dependent pressure profile.

For the results obtained without the influence of the human face, rotational symmetry occurs. The functions are therefore only dependent on the radius r. Hence, a combination of Gaussian distributions is proposed, i.e.

$$p(r) = \underbrace{A1 \cdot \exp^{-B1 \cdot r^2}}_{\text{Gaussian1}} - \underbrace{A2 \cdot \exp^{-B2 \cdot (r-r_c)^2}}_{\text{Gaussian2}}, \tag{2}$$

$$s(r) = \underbrace{A1 \cdot \exp^{-B1 \cdot r^{C1}}}_{\text{Gaussian1}} + \underbrace{A2 \cdot \exp^{-B2 \cdot (r-r_c)^2}}_{\text{Gaussian2}} - \underbrace{A1 \cdot \exp^{-B3 \cdot r^2}}_{\text{Gaussian3}}, \tag{3}$$

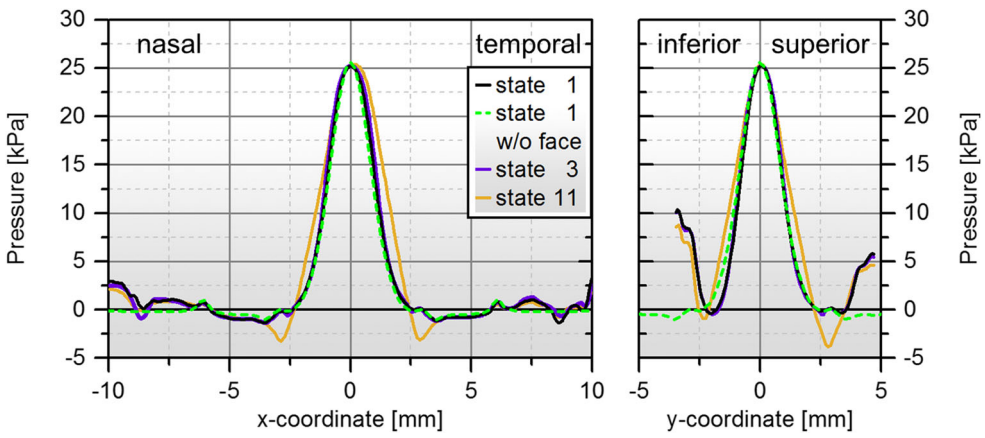

Fig. 8 The pressure distribution curves considering the human face for the most relevant deformation states along the nasal-temporal and inferior-superior section

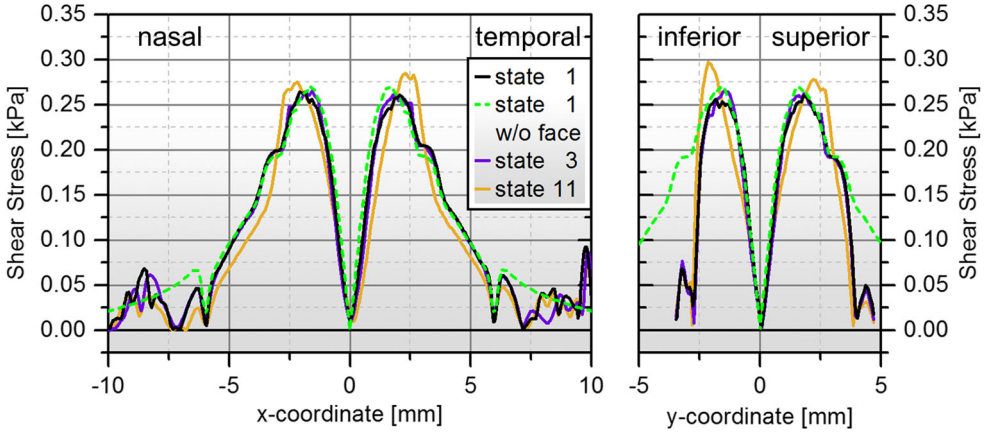

Fig. 9 Shear stress distribution curves considering the human face for the most relevant deformation states along the nasal-temporal and inferior-superior section

with p and s denoting the pressure and shear stress, respectively. The designed pressure distribution curve Eq. 2 consists of one Gauss curve representing the central pressure applied by the air puff and a subtracted Gauss function to consider the negative pressure at the peak of the deformation state. The shear distribution curve Eq. 3 consists of two superposed Gaussian curves, subtracting a third curve representing the central minimum. The obtained coefficients for each deformation state are presented in Table 4 for the pressure and Table 5 for the shear stress together with the related Pearson's correlation coefficient R. Furthermore, the deflection area DA is provided for the individual deformation states as an overall measure for the cornea deformation, which may be used to compare in an FE-calculation.

Naturally, the influence of the eyelid cannot be modeled by a two-dimensional equation, because the distributions are not rotationally symmetric. In order to account for this, the data is fit into nonlinear surfaces. The pressure distribution surface Eq. 4 consists of four Gaussian surfaces. One representing the central pressure applied by the air puff, a second subtracted Gaussian to consider the negative pressure in the peak of the deformed state and two more representing the increasing pressure evoked by the eyelids.

$$\begin{aligned} p(x,y) = & \underbrace{A1 \cdot \exp^{-abs\left(C1 \cdot x^2 + D1 \cdot y^2\right)}}_{\text{Gaussian1}} \\ & - \underbrace{A2 \cdot \exp^{-B2 \cdot abs\left(C1 \cdot x^2 + D1 \cdot y^2 + E_c^2 - 2 \cdot E_c \cdot \sqrt{C1 \cdot x^2 + D1 \cdot y^2}\right)}}_{\text{Gaussian2}} \\ & + \underbrace{A3 \cdot \exp^{-B3 \cdot abs\left(C3 \cdot x^2 + D3 \cdot (y - y_c)^2\right)}}_{\text{Gaussian3}} \\ & + \underbrace{A3 \cdot \exp^{-B3 \cdot abs\left(C3 \cdot x^2 + D3 \cdot (y + y_c)^2\right)}}_{\text{Gaussian4}}, \end{aligned} \tag{4}$$

with x and y denoting the nasal-temporal direction and inferior-superior direction, respectively. Equation 5 shows the designed surface representing the shear stress distribution. It consists, similar to the two-dimensional function, of three Gaussian surfaces, subtracted from each other and include 10 parameters per state.

$$\begin{aligned} s(x,y) = & \underbrace{A1 \cdot \exp^{-\left(C1 \cdot abs(x)^{E1} + D1 \cdot abs(y)^{E1}\right)}}_{\text{Gaussian1}} \\ & + \underbrace{A2 \cdot \exp^{-abs\left(C2 \cdot x^2 + D2 \cdot y^2 + E_c^2 - 2 \cdot E_c \cdot \sqrt{C2 \cdot x^2 + D2 \cdot y^2}\right)}}_{\text{Gaussian2}} \\ & - \underbrace{A1 \cdot \exp^{-abs\left(C3 \cdot x^2 + D3 \cdot y^2\right)}}_{\text{Gaussian3}} \end{aligned} \tag{5}$$

The obtained coefficients for each deformation state were presented in the Tables 6 and 7. Based on the used eyelid geometry, the equations and related coefficients are valid in the range according to Eq. 6.

$$0 \leq \frac{x^2}{10^2} + \frac{y^2}{4.7^2} \leq 1 \tag{6}$$

Table 3 Integrally based deviations between the undeformed levitating eye and the deformed states of the eye taking into account the human face

	Nasal-temporal		Inferior-superior	
State [−]	pressure f [%]	shear f [%]	pressure f [%]	shear f [%]
1	24.18	12.36	30.52	42.02
2	23.36	12.61	30.51	41.97
3	26.60	12.93	30.77	43.01
4	28.45	12.84	32.57	43.15
5	32.48	15.36	33.89	44.42
6	36.80	17.00	35.68	46.37
7	41.18	19.16	36.52	47.17
8	43.63	21.02	38.49	47.52
9	46.99	21.69	37.10	47.47
10	49.94	23.12	38.92	47.99
11	52.01	24.20	38.68	47.89

Table 4 Coefficients of the function Eq. 2 to describe the pressure applied on the cornea

		Cornea deformation states										
Coeff.	Unit	1	2	3	4	5	6	7	8	9	10	11
DA	mm^2	0	0.11	0.32	0.54	0.82	1.28	1.61	2.04	2.51	2.94	3.38
R	%	99.9	99.9	99.9	99.9	99.9	99.9	99.9	99.9	99.9	99.9	99.9
$A1$	Pa	25 133	25 133	25 133	25 133	25 133	25 133	25 133	25 133	25 133	25 133	25 133
$B1$	mm^{-2}	0.75	0.75	0.64	0.66	0.47	0.42	0.42	0.38	0.42	0.26	0.41
$A2$	Pa	0	0	1124	1305	3831	4451	4564	4715	3773	7072	4584
$B2$	mm^{-2}	0	0	1	3	1.49	1.32	1.15	0.91	1.07	0.67	1.94
r_c	mm	0	0	2.00	2.30	1.87	2.01	2.08	2.22	2.51	2.28	2.75

Table 5 Coefficients of the function Eq. 3 to describe the shear stress applied on the cornea

		Cornea deformation states										
Coeff.	Unit	1	2	3	4	5	6	7	8	9	10	11
DA	mm^2	0	0.11	0.32	0.54	0.82	1.28	1.61	2.04	2.51	2.94	3.38
R	%	99.4	99.4	99.5	99.5	99.5	99.4	99.3	99.4	99.4	99.4	99.4
$A1$	Pa	280	298	328	345	306	288	246	206	123	165	137
$B1 \cdot 10^3$	mm^{-C}	146	166	201	221	197	176	136	98	18	63	29
$C1$	–	1.27	1.22	1.15	1.12	1.15	1.19	1.27	1.38	2.00	1.54	1.84
$A2$	Pa	59	55	53	53	73	84	105	126	160	176	162
$B2 \cdot 10^3$	mm^{-2}	224	227	233	252	331	385	440	447	549	458	806
r_c	mm	1.58	1.58	1.58	1.59	1.80	1.80	1.85	1.91	2.17	1.90	2.31
$B3$	mm^{-2}	1.58	1.50	1.31	1.24	1.18	1.01	0.98	0.85	2.78	0.41	4.86

Table 6 Coefficients of the surface function Eq. 4 to describe the pressure load applied on the cornea with consideration of the human face

		Cornea deformation states										
Coeff.	Unit	1	2	3	4	5	6	7	8	9	10	11
DA	mm^2	0	0.11	0.32	0.54	0.82	1.28	1.61	2.04	2.51	2.94	3.38
R	%	86.7	87.0	88.9	89.1	90.3	91.5	92.3	92.8	93.5	93.8	94.5
$A1$	Pa	25 133										
$C1$	mm^{-2}	0.68	0.68	0.65	0.62	0.59	0.55	0.51	0.45	0.44	0.42	0.38
$D1$	mm^{-2}	0.89	0.90	0.87	0.85	0.79	0.72	0.66	0.63	0.61	0.59	0.52
$A2$	Pa	0	0	636	874	1756	2553	3137	3024	3137	3485	3853
$B2$	–	0	0	18.3	6.23	7.41	8.86	9.18	6.18	7.94	8.85	8.55
E_c	mm	0	0	2.13	2.05	1.91	1.84	1.75	1.75	1.82	1.86	1.74
$A3$	Pa	5219	5234	5120	5111	5095	4976	5003	5002	4958	4914	4845
$B3$	–	1.43	1.45	1.96	2.32	2.23	1.20	0.98	0.56	0.48	0.40	0.29
$C3 \cdot 10^4$	mm^{-2}	1.58	7.47	6.89	7.49	10.5	23.8	38.1	86.8	131	244	333
$D3$	mm^{-2}	0.71	0.69	0.50	0.43	0.44	0.82	1.03	1.81	2.16	2.64	3.73
y_c	mm	4.7										

Table 7 Coefficients of the surface function Eq. 5 to describe the shear stress applied on the cornea with consideration of the human face

		Cornea deformation states										
Coeff.	Unit	1	2	3	4	5	6	7	8	9	10	11
DA	mm^2	0	0.11	0.32	0.54	0.82	1.28	1.61	2.04	2.51	2.94	3.38
R	%	95.0	95.1	95.1	95.2	95.1	95.2	95.4	95.7	95.9	96.2	96.2
$A1$	Pa	89.6	64.3	131	140	144	241	260	172	175	185	150
$C1 \cdot 10^3$	mm^{-E1}	11.4	5.4	15.2	18.4	17.6	21.8	28.0	12.8	12.9	17.3	13.4
$D1 \cdot 10^3$	mm^{-E1}	22.4	12.3	35.4	41.0	38.0	48.7	59.1	30.6	30.4	37.7	31.1
$E1$	–	2.23	2.44	2.30	2.21	2.26	2.39	2.29	2.56	2.59	2.46	2.52
$A2$	Pa	169	192	145	143	145	84.5	111	135	136	140	159
$C2$	mm^{-2}	0.25	0.19	0.22	0.25	0.31	1.58	0.49	0.80	1.16	1.51	1.06
$D2$	mm^{-2}	0.44	0.34	0.36	0.39	0.50	1.81	0.52	1.03	1.47	1.84	1.31
E_c	mm	1.12	0.90	0.89	0.93	1.10	2.50	1.47	1.90	2.45	2.84	2.41
$C3$	mm^{-2}	2.41	1.19	0.91	0.83	0.83	1.00	0.87	1.06	1.75	1.79	2.47
$D3$	mm^{-2}	2.41	1.26	1.23	1.11	1.05	1.45	1.30	1.35	2.66	2.90	4.61

For implementation, a stepwise simulation of the cornea deformation during an NCT examination is recommended. In each step, the stress distribution following the proposed equations has to be applied, wherein those parameters are chosen which are according to the deflection area from the previous step. Then, the resulting deformed state is calculated as data for the next step.

Discussion

A quick, early and safe diagnosis of eye diseases such as keratoconus or glaucoma is essential for early treatment to minimize their effects on vision. The determination of biomechanical parameters based on NCT examinations offers an opportunity to enable such diagnoses in the future. In addition to the diagnosis of diseases, it is also important to be able to detect biomechanically weak corneas of already diseased candidates to exclude them from refractive corneal surgery. To determine the necessary biomechanical parameters, the external loads acting on the eye and the resulting deformations are required. In this publication, the authors presented a new approach for the determination and calibration of the air puff generated by Corvis ST. The method includes inverse modeling combined with experimentally determined data. A maximum pressure at the nozzle inlet of $p_{\text{inlet}} \approx 25\,\text{kPa}$ (188.5 mmHg) was identified. Furthermore, it was shown that the losses between the nozzle inlet and the corneal surface are low, so that the maximum stagnation pressure on the corneal surface almost corresponds to the maximum pressure at the nozzle inlet. Compared to the results of previous studies, which are summarized in Table 8, the present results confirm the approaches of Roy and Ariza-Garcia but are higher than those of Bahr, Kling and Metzler. Metzler et al. [11] characterized the air puff with a hot-wire anemometer and described a peak velocity at the nozzle outlet of over 100 m/s. Maybe this result is based on exceeding the measuring range or the measuring rate of the sensor used is not high enough to record the rapid speed change within the 30 ms. Calculating the dynamic pressure from this speed using the Bernoulli equation Eq. 7, at an air density of $\rho = 1.204\,\text{kg/m}^3$ at 20 °C [24] gives a pressure of $p = 6\,\text{kPa}$. This is smaller than the pressure determined in the current work, so that conversely the speed is higher than 100 m/s. The outcome thus confirms Metzler's [11] assumption. Kling et al. [15] measures pressure with an MPX2301DT1 sensor from Freescale Semiconductors Inc. at a typical Corvis ST measurement distance of 11 mm. This sensor has an active surface with a diameter between 2.41 mm and 2.72 mm [25]. It follows that the sensor averages the pressure over the active surface, so that the sensor underestimates the maximum pressure in the air puff center, which could explain why the pressure determined in this way is lower than the pressure obtained here. Bahr et al. [14] chooses his model condition according to the

Table 8 Overview of the characteristics of the air puff assumed or determined by other groups

Main author	p_{Inlet} [kPa] ([mmHg])	p_{Cornea} [kPa] ([mmHg])	Year [−]	Reference
Metzler	–	> 6 (>45)	2013	[11]
Kling	–	≈ 16 (≈ 120)	2014	[15]
Bahr	–	≈ 2.3 (≈ 17)	2015	[14]
Ariza-Garcia	–	25 (≈ 188)	2015	[12]
Roy	≈24 (≈ 180)	–	2015	[13]

Corivs ST operating manual [26], which has few physical motivation. Ariza-Garcia [12] and Roy [13] assumed in their CFD simulations that the pressure at the nozzle inlet or outlet is equal to the pressure measured with the Corvis ST internal sensor without performing an experimental validation. In this investigation, the loss of kinetic energy between the pressure chamber and the sensor as well as between the chamber and the nozzle inlet was found to be almost identical. The experimental data also showed that the time response of the pressure on the cornea is similar to the pressure-time curve measured with the Corvis ST internal pressure sensor. Thus, approaches using chamber pressure as a boundary condition were justified by this investigation.

$$p = \frac{\rho}{2} v^2 \tag{7}$$

The investigations also show that external loads acting on a cornea depend on the current state of deformations, which confirms results already shown by Kling et al. [15]. The deformation based deviations between the pressure distribution curves calculated using Eq. 1 are up to approx. 34 % and between the shear stress distribution curves up to approx. 14 %. The novelty of the results compared to previous publications is the use of real measured, deformed corneal contours for the investigations. In addition, this work investigated the influence of the human face that surrounds the eye. It has been shown that the eyelids have an influence on the distribution of pressure and shear forces and that the assumption of a rotationally symmetric load is not appropriate. The effects caused by the eyelids increase the relative deviations between the pressure distribution curves to about 52 % in the nasal-temporal and 39 % in the inferior-superior cut. The relative deviations between the shear stress distribution curves were increased to approximately 24 % in the nasal-temporal cut and 48 % in the inferior-superior cut.

Conclusion

Based on the assumption that the air puff generated by the Corvis ST is identical for each device in every investigation, the authors have proposed a mathematical description of the stress distribution depending on different deformation states. Note that the stress distributions provided apply to the eye and face geometry used in the paper. In the present work, an experimental characterization of the air puff created by the Corvis ST in combination with a computational fluid dynamic simulation was done. It was shown that the nozzle inlet pressure at the Corvis ST is approximately equal to the pressure measured with the internal pressure sensor of the device, so that possible losses are insignificant. Also the deceleration of the flow between the nozzle outlet and the cornea is negligible. From this, it can be concluded that the influence of a distance change between eye and nozzle outlet is also insignificantly small due to a possible whole eye movement. After characterizing the air puff, a numerical influence study of the interaction between the air puff and the cornea deformation showed that the distribution of pressure and shear stress clearly depends on the deformation state of the cornea. An exception are the very similar undeformed and applanated deformation states, which have approximately the same pressure and shear stress distributions. The shear stresses on the cornea produced by the air puff are one hundred times smaller than the pressure. Note, that this not necessarily means an insignificance of the shear stresses. Future researches should examine the influence of variations in the cornea or eyelid geometry.

Acknowledgements The authors appreciate financial funding from the European Research Fund (ESF) through the training research group "Cosima" (ESF Project 100231947). Furthermore, the author Daniel Balzani thanks the Institutional Strategy "The Synergetic University" at Technische Universität Dresden funded by the DFG and the author Eberhard Spörl appreciates funding from the Ministry of Education and Research for a German-India project. The funders had no role in study design, data collection and analysis, decision to publish, or preparation of the manuscript.

References

1. Vaughan JM, Randall JT (1980) Brillouin scattering, density and elastic properties of the lens and cornea of the eye. Nature 5755:489–491. https://doi.org/10.1038/284489a0
2. Hollman KW, Emelianov SY, Neiss JH, Jotyan G, Spooner GJR et al (2002) Strain imaging of corneal tissue with an ultrasound elasticity microscope. Cornea 1:68–73. https://doi.org/10.1097/00003226-200201000-00015
3. Luce DA (2005) Determining in vivo biomechanical properties of the cornea with an ocular response analyzer. J Cataract Refract Surg 1:156–162. https://doi.org/10.1016/j.jcrs.2004.10.044
4. Jaycock PD, Lobo L, Ibrahim J, Tyrer J, Marshall J (2005) Interferometric technique to measure biomechanical changes in the cornea induced by refractive surgery. J Cataract Refract Surg 1:175–184. https://doi.org/10.1016/j.jcrs.2004.10.038
5. Ford M, Dupps WJ Jr, Huprikar N, Lin R, Rollins AM (2006) OCT corneal elastography by pressure-induced optical feature flow. Proc SPIE 6138:61380P-61380P-7. https://doi.org/10.1117/12.648685
6. Litwiller DV, Pulido JS, Kruse SA, Glaser KJ, Ehman RL (2007) MR elastography of the eye: initial feasibility. Proc Intl Soc Mag Reson Med 15:1262
7. Tanter M, Touboul D, Gennisson JL, Bercoff J, Fink M (2009) High-resolution quantitative imaging of cornea elasticity using supersonic shear imaging. IEEE Trans Med Imaging 12:1881–1893. https://doi.org/10.1109/TMI.2009.2021471
8. Li C, Guan G, Huang Z, Johnstone M, Wang RK (2012) Noncontact all-optical measurement of corneal elasticity. Opt Lett, OSA 10:1625–1627. https://doi.org/10.1364/OL.37.001625
9. Elsheikh A, Alhasso D, Kotecha A, Garway-Heath D (2009) Assessment of the ocular response analyzer as a tool for intraocular pressure measurement. J Biomed Eng, ASME 8:081010-1–081010-9. https://doi.org/10.1115/1.3148462

10. Whitford C, Studer H, Boote C, Meek KM, Elsheikh A (2015) Biomechanical model of the human cornea: Considering shear stiffness and regional variation of collagen anisotropy and density. J Mech Behav Biomed 42:76–87. https://doi.org/10.1016/j.jmbbm.2014.11.006
11. Metzler K, Roberts C, Whitaker S, Lawrence M, Malik J, Bons J (2013) Modeling corneal response to an air puff using deformation data to derive Young's modulus. Invest Ophthalmol Vis Sci 15:1629
12. Ariza-Gracia MÁ, Zurita JF, Piñero DP, Rodriguez-Matas JF, Calvo B (2015) Coupled biomechanical response of the cornea assessed by non-contact tonometry. A simulation study. PLoS ONE 3:1–15. https://doi.org/10.1371/journal.pone.0121486
13. Roy AS, Kurian M, Matalia H, Shetty R (2015) Air-puff associated quantification of non-linear biomechanical properties of the human cornea in vivo. J Mech Behav Biomed 48:173–182. https://doi.org/10.1016/j.jmbbm.2015.04.010
14. Bahr N, Ali N, Patel D, McGhee C, Hunter P et al (2015) Modelling the deformation of the human cornea produced by a focussed air pulse. In: Doyle B, Miller K, Wittek A, Nielsen PM (eds) Computational biomechanics for medicine: New approaches and new applications. Springer International Publishing, pp 93–100. https://doi.org/10.1007/978-3-319-15503-6_9
15. Kling S, Bekesi N, Dorronsoro C, Pascual D, Marcos S (2014) Corneal viscoelastic properties from finite-element analysis of in vivo air-puff deformation. PLoS ONE 8:1–12. https://doi.org/10.1371/journal.pone.0104904
16. Muench S, Balzani D, Roellig M, Spoerl E (2017) Method for the development of realistic boundary conditions for the simulation of non-contact tonometry. PAMM 17:207–208. https://doi.org/10.1002/pamm.201710073
17. Micro-Epsilon Messtechnik GmbH & Co. KG (2011) Instruction Manual optoNCDT 2300
18. Menter FR (1994) Two-equation eddy-viscosity turbulence models for engineering applications. AIAA-J 8:1598–1605. https://doi.org/10.2514/3.12149
19. (2015) ANSYS Release16.1, ANSYS Documentation CFX, Theory Guide, 11.1.1 Discretization of the Governing Equations, ANSYS, Inc.
20. VDI/VDE (1993) 2640 Netzmessungen in Stroemungsquerschnitten (Blatt1): Allgemeine Richtlinien und mathematische Grundlagen. VDI-Verlag
21. Celik IB, Ghia U, Roache PJ, Freitas CJ, Coleman H et al (2008) Procedure for estimation and reporting of uncertainty due to discretization in CFD applications. J Fluid Eng-T ASME 7:078001-1–078001-4. https://doi.org/10.1115/1.2960953
22. Werkmeister RM, Alex A, Kaya S, Unterhuber A, Hofer B et al (2013) Measurement of tear film thickness using ultrahigh-resolution optical coherence tomography. Invest Ophthalmol Vis Sci 8:5578–5583. https://doi.org/10.1167/iovs.13-11920
23. XAMR. Human Head. Grabcad. [Online] Available at: https://grabcad.com/library/human-head-1 [Accessed 21 April 2016]
24. U.S. (1962) Committee on Extension to the Standard Atmosphere U.S. Standard Atmosphere 1962. U.S Government Printing Office, Washington D.C
25. Freescale Semiconductor (2012) Data Sheet: Technical Data MPX2300DT1. Rev 9
26. Oculus Optikgeraete GmbH (2011) Corvis ST instruction manual